Corrected 29 January 2018. See full text.

MAGNETIC MATERIALS

Chiromagnetic nanoparticles and gels

Jihyeon Yeom,[1,2] Uallisson S. Santos,[3] Mahshid Chekini,[2,4] Minjeong Cha,[2,5]
André F. de Moura,[3]* Nicholas A. Kotov[1,2,4,5,6]*

Chiral inorganic nanostructures have high circular dichroism, but real-time control of their optical activity has so far been achieved only by irreversible chemical changes. Field modulation is a far more desirable path to chiroptical devices. We hypothesized that magnetic field modulation can be attained for chiral nanostructures with large contributions of the magnetic transition dipole moments to polarization rotation. We found that dispersions and gels of paramagnetic Co_3O_4 nanoparticles with chiral distortions of the crystal lattices exhibited chiroptical activity in the visible range that was 10 times as strong as that of nonparamagnetic nanoparticles of comparable size. Transparency of the nanoparticle gels to circularly polarized light beams in the ultraviolet range was reversibly modulated by magnetic fields. These phenomena were also observed for other nanoscale metal oxides with lattice distortions from imprinted amino acids and other chiral ligands. The large family of chiral ceramic nanostructures and gels can be pivotal for new technologies and knowledge at the nexus of chirality and magnetism.

Optical materials that combine chirality and magnetism are essential for spintronics, magneto-optics, magnetochemistry, and chiral catalysts (*1*, *2*) because they allow modulation of light beams, excited states, and chemical processes by means of a magnetic field. The junction of chirality and magnetism is central to skyrmions, spin catalysis, and the origin of homochirality in life on Earth (*3*–*5*), representing some of the newly emerged and long-standing problems of physics, chemistry, and biology. For all of these physicochemical phenomena, it is essential to increase the coupling of the photon's magnetic field with magnetic moments of electrons in chiral matter, which is expected to markedly enhance the chiroptical activity and first- and second-order magneto-optical phenomena, such as the Faraday effect, magnetic circular dichroism, and magneto-chiral dichroism (*6*–*12*). However, optical materials that combine a large magnetic moment and chiral asymmetry are rare (*13*). The common examples of such materials that can be dubbed chiromagnetic are typically based on complexes of transition metals (*14*, *15*). But even for optical centers with rare-earth f orbitals accommodating multiple unpaired spins, the long-distance spin coupling enhancing the magnetic field effect on electronic transitions requires low temperatures of $T = 5$ to 7 K (*14*, *15*).

Chiral inorganic nanoparticles (NPs) (*16*–*19*) and their assemblies (*12*, *20*) provide a new toolbox for the design of materials combining chirality and magnetism. Whereas the optical transitions in rare-earth coordination compounds involve localized molecular orbitals, the optical transitions in NPs may engage orbitals involving thousands of atoms, and so does their chirality (*21*). Unlike coordination compounds, the optical "center" responsible for chiroptical properties in inorganic NPs becomes orders of magnitude greater in volume compared with coordination compounds from f metals; magnetic coupling between atomic spins is also facilitated by shorter distances between magnetic atoms. Importantly, the chiral NPs may also show distorted crystal lattices (*22*, *23*) and exhibit (super)paramagnetism (*12*, *24*–*26*). This set of NP characteristics enables enhancement and spectral tuning of multiple chiroptical properties. (*27*, *28*) In this study, we focus on the first-order effects of magnetic field on light absorption and circular dichroism (CD). The importance of magnetic properties of NPs for absorption of circularly polarized photons can be easily inferred from the quantum mechanical parameter known as rotational strength, R_{0a}, which can be calculated as

$$R_{0a} = \mathrm{Im}[\langle\Psi_0|\hat{\boldsymbol{\mu}}|\Psi_a\rangle \cdot \langle\Psi_a|\hat{\mathbf{m}}|\Psi_0\rangle] = \mathrm{Im}[\boldsymbol{\mu}_{0a} \cdot \mathbf{m}_{a0}] \qquad \text{(Eq. 1)}$$

where Ψ_0 and Ψ_a are the wave functions for the ground state (0) and excited state (a), $\hat{\boldsymbol{\mu}}$ and $\hat{\mathbf{m}}$ are the corresponding electric and magnetic moment operators, and $\boldsymbol{\mu}_{0a}$ and $\mathbf{m}_{a0}$ are the electric and magnetic transition dipole moments, respectively (*6*, *9*). Equation 1 holds true for any and all quantum systems, whether chiral or not, whether bearing unpaired electrons or not, and whether in the presence of an external magnetic field or not (*8*, *29*). As applied to chiral materials, Eq. 1 is usually simplified at the expense of the magnetic term (*6*–*9*, *30*). For instance, in the case of plasmonic NPs, the magnetic moment term is reduced to a small constant, whereas the electric moment term is considered to be most essential (*6*). However, in NPs with a large number of unpaired electrons and a chiral crystal lattice, the magnetic moment term $\langle\Psi_a|\hat{\mathbf{m}}|\Psi_0\rangle$ should have a contribution comparable to that of the electric moment term $\langle\Psi_0|\hat{\boldsymbol{\mu}}|\Psi_a\rangle$, which should lead to enhanced R_{0a} and potentially to practical realizations of NP chirality in magneto-optical devices operating at low fields and ambient temperatures.

Equally importantly, the large CD observed, for instance, for chiroplasmonic assemblies was difficult to translate to chiroptical devices, because all known approaches for real-time modulation of their optical activity are associated with irreversible chemical changes in the NP systems (*31*–*37*). At the same time, the helical assemblies of magnetic NPs are not known in the enantioselective form (*38*).

To address this set of fundamental and technological questions, we synthesized ~5-nm Co_3O_4 NPs using the L- and D-enantiomers of cysteine (Cys) as surface ligands. These NPs serve as the primary experimental model in this study and will be referred to as D-, L-, and DL-Cys Co_3O_4 when the corresponding Cys enantiomers or their equimolar mixture were used for NP synthesis. The choice of cobalt oxide as the inorganic core of the NPs was governed by its known magnetism and structural versatility, as well as the environmental robustness of cobalt-based ceramics. The chemical structure and atomic composition of the NPs was established by x-ray photoelectron spectroscopy (fig. S1, A to C) and atomic mapping (fig. S2) (*39*). Transmission electron microscopy (TEM) and scanning transmission electron microscopy (STEM) indicated the frequent presence of NPs with a seemingly amorphous inorganic phase (fig. S1, D to F). When the crystal structure was observed, the lattice plane distances could be adequately described by those in the cubic spinel phase. The crystalline domains are confined to the central part of the NPs, indicating that the seemingly amorphous shells originate from the crystal lattice distortions in the vicinity of the NP surface caused by molecular imprinting from attached enantiomers of amino acids. Instead of the typical antiferromagnetic behavior of Co_3O_4 nanostructures (*40*, *41*) owing to exchange interactions in the spinel lattice, these NPs exhibit paramagnetic behavior even below the Néel temperature expected for Co_3O_4 (fig. S1, G to J); this observation confirms that crystal lattice distortions are characteristic of the vast majority of the NPs in the ensemble formed in this synthesis.

The brown transparent dispersions of these NPs yield CD spectra of high intensity, with up to eight positive and negative peaks in the ultraviolet (UV) and visible range (Fig. 1, A and C) corresponding to various transitions [intraparticle $Co(II) \rightarrow Co(III)$ (230, 280, and 350 nm) and surface states (including ligands)$\rightarrow Co(III)$ (450, 550, and 600 nm)], as demonstrated by the simplified time-dependent density functional theory (*42*, *43*) calculation of a model NP (fig. S7 and table S1). The CD spectra for D- and L-Cys Co_3O_4 showed a nearly perfect mirror symmetry, whereas Co_3O_4 NPs made with equal amounts of D- and L-Cys were chiroptically silent (Fig. 1A). The spectral

---

[1] Department of Macromolecular Science and Engineering, University of Michigan, Ann Arbor, MI 48109, USA. [2] Biointerfaces Institute, University of Michigan, Ann Arbor, MI 48109, USA. [3] Department of Chemistry, Federal University of São Carlos, 13.565-905, São Carlos, São Paulo, Brazil. [4] Department of Chemical Engineering, University of Michigan, Ann Arbor, MI 48109, USA. [5] Department of Materials Science and Engineering, University of Michigan, Ann Arbor, MI 48109, USA. [6] Department of Biomedical Engineering, University of Michigan, Ann Arbor, MI 48109, USA.
***Corresponding author. Email: moura@ufscar.br (A.F.d.M.); kotov@umich.edu (N.A.K.)**

Corrected 29 January 2018. See full text.

positions of the CD peaks were nearly perfectly aligned with those in absorption (Fig. 1C). Chiroptical anisotropy *g*-factors as high as 0.02 were obtained (Fig. 1B), which is ~10 times those obtained for other NPs of similar size, including plasmonic ones with known strong chiroptical activity (*44*, *45*). The high value of the *g*-factor in the visible range can also be appreciated by the naked eye as the appearance of a distinct color when light passes through the NP-polyacrylamide gel and between crossed polarizers (Fig. 1D and scheme S1) (*31*); the green color corresponds to the 550-nm peak in the *g*-factor spectra in Fig. 1B.

The strong chiroptical activity was also observed for Co_3O_4 NPs synthesized and capped by L- and D-penicillamine, but CD peaks were at different positions (fig. S11) than those for Cys, especially for the visible range. Importantly, little change in the CD spectra was observed when Cys ligands were exchanged for penicillamine after the formation of NPs (fig. S12), indicating that chiroptical activity in the range of ~400 to 700 nm is associated with the inorganic core of NPs. Conservation of NP chirality after the ligand exchange is consistent with observations of chiral memory (*46*) and the high activation barrier for reconstruction of the Co_3O_4 lattice once NPs are formed. The kinetic stability of the chiral distortions also provides a pathway to other chiral nanostructures from Co_3O_4 by means of self-assembly using ligand-depleted NPs (*9*).

Raman scattering spectra further validated the chirality of the inorganic cores in the NPs. Characteristic bands at 380, 475, 516, 613, and 680 cm^{-1} observed for D- and L-Cys Co_3O_4 NPs are associated with Raman-active vibration modes of Co_3O_4 (Fig. 2C) (*47*). Raman optical activity spectra show peaks of opposite polarity at 377, 465, 531, and 719 cm^{-1} for the NPs carrying opposite enantiomers of Cys (Fig. 2D). Of particular importance is the strong peak at 380 cm^{-1} that corresponds to lattice phonons of Co_3O_4. It occurs at frequencies higher than expected for Co_3O_4 with the cubic spinel crystal lattice (*47*) and shows a distinct antisymmetric relation of these vibrations in Co_3O_4 carrying L- and D-Cys (*48*). Both facts indicate the chirality transfer from amino acids to the crystal lattice of the inorganic core of the NPs, manifesting as crystal lattice distortions (*49*) propagating from the surface of the NPs into the core, which can also be seen in STEM images (fig. S1, E and F).

Computational study of atomic-scale dynamics in Co_3O_4 NPs having either L- or D-Cys on the surface were carried out to better understand the nature of the chirality transfer and distortions in the NP core. Relatively small NPs with Cys residues that were coordinated identically with experimental NPs were used in the simulations (fig. S6). In the course of full structural optimization, emblematic chiral geometries with mirror-image symmetries independently evolved for L- and D-Cys–bearing NPs. Specifically, three ligands on each corner of the tetrahedral model NP formed ringlike structures with either a clockwise or a counterclockwise sense of rotation with respect to the C_3 axis (Fig. 2, A and B). Using the Cahn-Ingold-Prelog system, they can be classified as *M* (clockwise) and *P* (counterclockwise) enantiomers. Taking into account the hierarchical chirality in these structures that arises from superposition of the molecular chirality of the amino acids and their orientation on the surface, they can be denoted as *M*-D-Cys and *P*-L-Cys Co_3O_4 NPs.

The normal-mode analysis of the model NP indicated that peaks at 505, 529, 601, and 693 cm^{-1} correspond to the Raman active breathing mode of the inorganic core and ligand-core coupling (fig. S14). The experimental peaks in Fig. 2C match calculations for the *M*-D-Cys and *P*-L-Cys NPs well, with many of the bands representing the coupled vibrations of the surface atoms and ligands (movies S1 to S4).

In the ab initio molecular dynamics (AIMD) simulations, both enantiomers evolved independently, as demonstrated by the energy fluctuations of each model (fig. S19). Concomitantly, the degree of chirality increased by fourfold as determined by the Hausdorff chirality measure (*50*) for both the *M*-D- and *P*-L-Cys NPs (Fig. 2E), indicating that thermal fluctuations increase the degree of distortion of the NPs. Notably, even when subjected to all of these vibrational distortions and bond reorganizations, the two model NPs followed nearly mirrored paths during the entire course of the AIMD simulations (Fig. 2F and movie S5).

MD simulations make it possible to follow the distortions being caused by the surface ligands in the ceramic crystal lattice. The NPs cores carrying L and D surface ligands present a pair of nearly mirrored structures after 2000 fs of structural relaxation (Fig. 3, B and C, and fig. S20, A and B). It is possible to analyze selected dihedral angles in these structures with respect to the value for the ideal crystallographic packing of Co_3O_4 cubic spinel (Fig. 3A). The three dihedral angles that we chose—$\phi_{35\text{-}15\text{-}8\text{-}18}$, $\phi_{35\text{-}12\text{-}11\text{-}22}$, and $\phi_{35\text{-}13\text{-}14\text{-}27}$—share O atom number 35, located at the center of one of the faces of the NP model (Fig. 3, A to C, and fig. S21, C and D), and have values $\phi_{35\text{-}15\text{-}8\text{-}18} = \phi_{35\text{-}12\text{-}11\text{-}22} = \phi_{35\text{-}13\text{-}14\text{-}27} = 0$ in the undistorted cubic spinel of Co_3O_4. The binding of the surface ligands led to noncoplanarity of these atoms that was already evident in the energy-minimization step, and these distortions increased

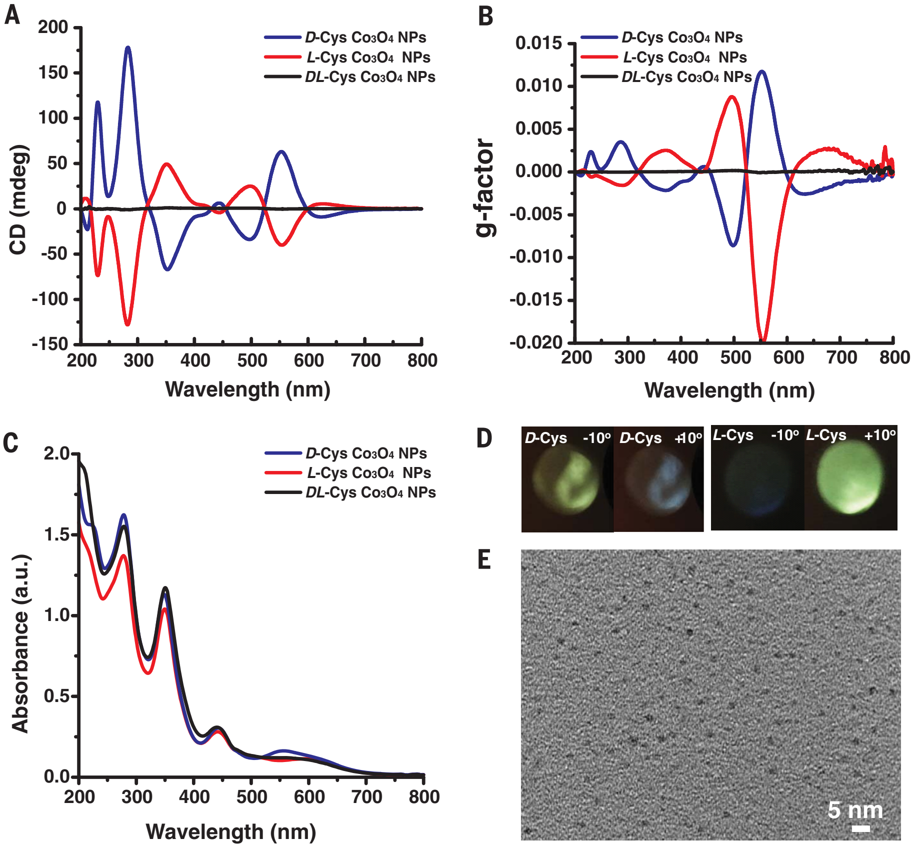

Fig. 1. Synthesized chiral Co_3O_4 NPs. (**A**) Circular dichroism (CD), (**B**) *g*-factor, defined as the ratio between the molar circular dichroism Δε and the molar extinction coefficient ε($g = \Delta\varepsilon/\varepsilon$), and (**C**) UV-visible absorption spectra of Co_3O_4 NPs stabilized by D-Cys, L-Cys, and DL-Cys. (**D**) Photographs of light transmitting through the NPs, with the rotation of the linear analyzer counterclockwise (−10°), and clockwise (+10°). (**E**) TEM image of L-Cys–capped Co_3O_4 NPs. mdeg, millidegrees; a.u., arbitrary units.

Corrected 29 January 2018. See full text.

during MD simulation. The mutual correlation of these angles stemming from the concerted movement of all the atoms in the nanoscale structures can be determined using Ramachandran-like plots. Similarly to proteins and other biomolecules, the pairwise probabilities of $\phi_{35\text{-}15\text{-}8\text{-}18}$, $\phi_{35\text{-}12\text{-}11\text{-}22}$, and $\phi_{35\text{-}13\text{-}14\text{-}27}$ acquiring specific values display unmistakable cross-correlation in the MD trajectories (Fig. 3, D to I). Importantly, the pattern of distortion is mirrored for D- and L-Cys NPs. These plots and MD simulations show the mechanism of chirality transfer in Co_3O_4 NPs that occurs during the growth of the NPs.

Chiral distortion of the original cubic spinel lattice changes the local magnetic fields within Co_3O_4 NPs because the overlap between atomic orbitals of Co^{3+} and O^{2-} and lattice symmetry are changed (*51*). Instantiating this point, the spin population of two Co(III) atoms changed from near zero to about two (tables S8 and S11) upon geometry optimization, owing to the distortions. The large spin and orbital angular momenta with corresponding operators $\hat{S}$ and $\hat{L}$ contribute to the chiroptical activity of NPs, according to Eq. 1, via magnetic transition dipole moments with the corresponding operator taking the form

$$\hat{\mathbf{m}} = \frac{-e\hbar}{2mc}(\hat{L} + g_S\hat{S}) \qquad \text{(Eq. 2)}$$

where g_S is the gyromagnetic ratio for spin angular momentum, m is electron mass, c is the speed of light, and h is the reduced Planck constant. Unusually high g-factors can only result from large $|\mathbf{m}|$ ($\mathbf{m}$-allowed) and small $|\boldsymbol{\mu}|$ ($\boldsymbol{\mu}$-forbidden) and either parallel ($\theta = 0°$) or antiparallel ($\theta = 180°$) orientations of the transient electrical and dipole moments (*52*). This is indeed the case for bands at 500, 550, and 650 nm (Fig. 1B) associated with the surface states of NPs, which provides direct experimental evidence for a strong contribution of magnetic transition dipole moments and paramagnetic enhancement of the optical activity of Co_3O_4 NPs. Naked-eye visualization of the large g-factors characteristic of Co_3O_4 NPs for an optical system with crossed polarizers indicates their importance for information technologies and photonics (Fig. 1D).

The key role of magnetically coupled unpaired electrons of Co atoms for the chiroptical activity of NPs was further confirmed by synthesizing mixed-metal NPs that included Cu^{2+} ions. Because the number of unpaired electrons in the NPs with Cu^{2+} was smaller than in those with neat Co_3O_4, magnetic transition dipole moments should be lower according to Eq. 2. Indeed, the g-values gradually decreased as the amount of Cu^{2+} increased (fig. S22).

In addition to Co-Cu mixed oxides, the generality of the magnetic effects on the chiroptical activity of NPs was confirmed for chiral nickel(II) oxide NPs that also showed strong optical activity with g-factors up to 0.01 (fig. S23). These NPs were similar in size, shape, and magnetic properties (figs. S24 to S26) to the Co_3O_4 NPs in Fig. 1.

As one would expect from Eqs. 1 and 2, the rotatory optical activity of D- and L-Cys NPs could be altered by the external magnetic field. To test magnetic field effects, the Co_3O_4 NPs were encapsulated in the transparent polyacrylamide gel (Fig. 4C) to avoid variation of optical properties owing to translational movement of the NPs. The NP gels showed the same optical and chiroptical bands at the same wavelengths in zero field as the NP dispersion (Fig. 4 and fig. S27). The magnetic field effect manifested as (i) a dramatic increase in UV transparency for circularly polarized light and (ii) its disappearance for racemic DL-Cys NPs (fig. S28), which is fundamentally different than the magnetic circular dichroism (MCD) that has been found for Au, Ag, or Fe_3O_4 NPs (*53*–*56*). Importantly, the field-on/field-off ratios for 280-nm NP absorption peaks of left and right circularly polarized beams and their sum (Fig. 4, A and B) markedly exceed the ratios for even the giant Faraday rotation found in nanoscale plasmonic systems (*19*, *20*, *57*) and giant Zeeman splitting (*58*, *59*). Also, the chiroptical effects of this magnitude were observed for D- and L-Cys NPs at room temperature, as opposed to the liquid helium temperatures often used for experimental observations of chiroptical effects in magnetic nanomaterials (*14*, *15*) and the magnetooptical effects mentioned above.

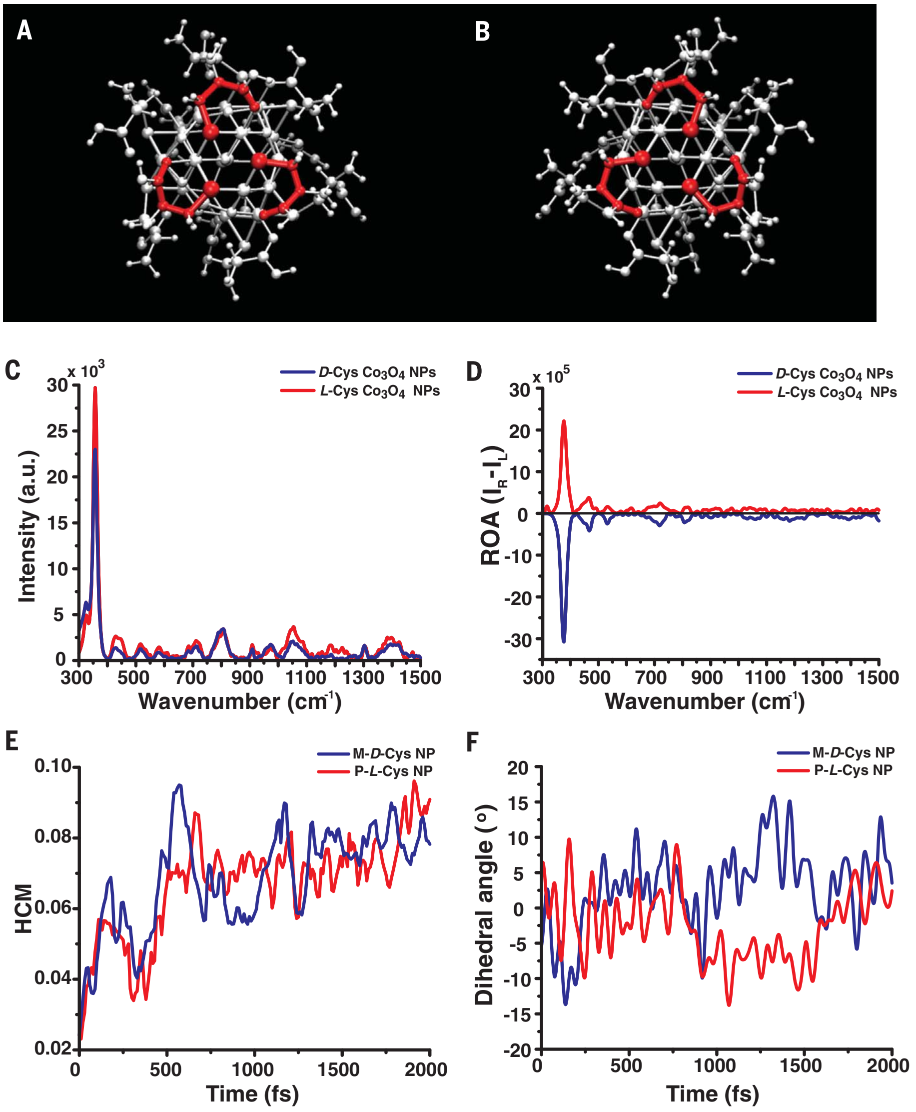

Fig. 2. Rotations of crystalline structures. (**A** and **B**) D-Cys (A) and L-Cys (B) Co_3O_4 NPs. Sulfur atoms are the larger red spheres forming one corner of the tetrahedra, and the remaining atoms depicted in red are C–C–C–O from the Cys ligands. (**C** and **D**) Raman (C) and Raman optical activity (ROA) (D) backscattering spectra with 532-nm excitation of D-Cys and L-Cys Co_3O_4 NPs in scattered circular polarization ROA mode. These spectra are courtesy of BioTools. (**E**) Hausdorff chirality measure (HCM) for the NP cores. (**F**) Dihedral angles between atoms 18, 7, 9, and 22 [O–Co(III)–Co(III)–O] of L-Cys and D-Cys Co_3O_4 NPs.

Corrected 29 January 2018. See full text.

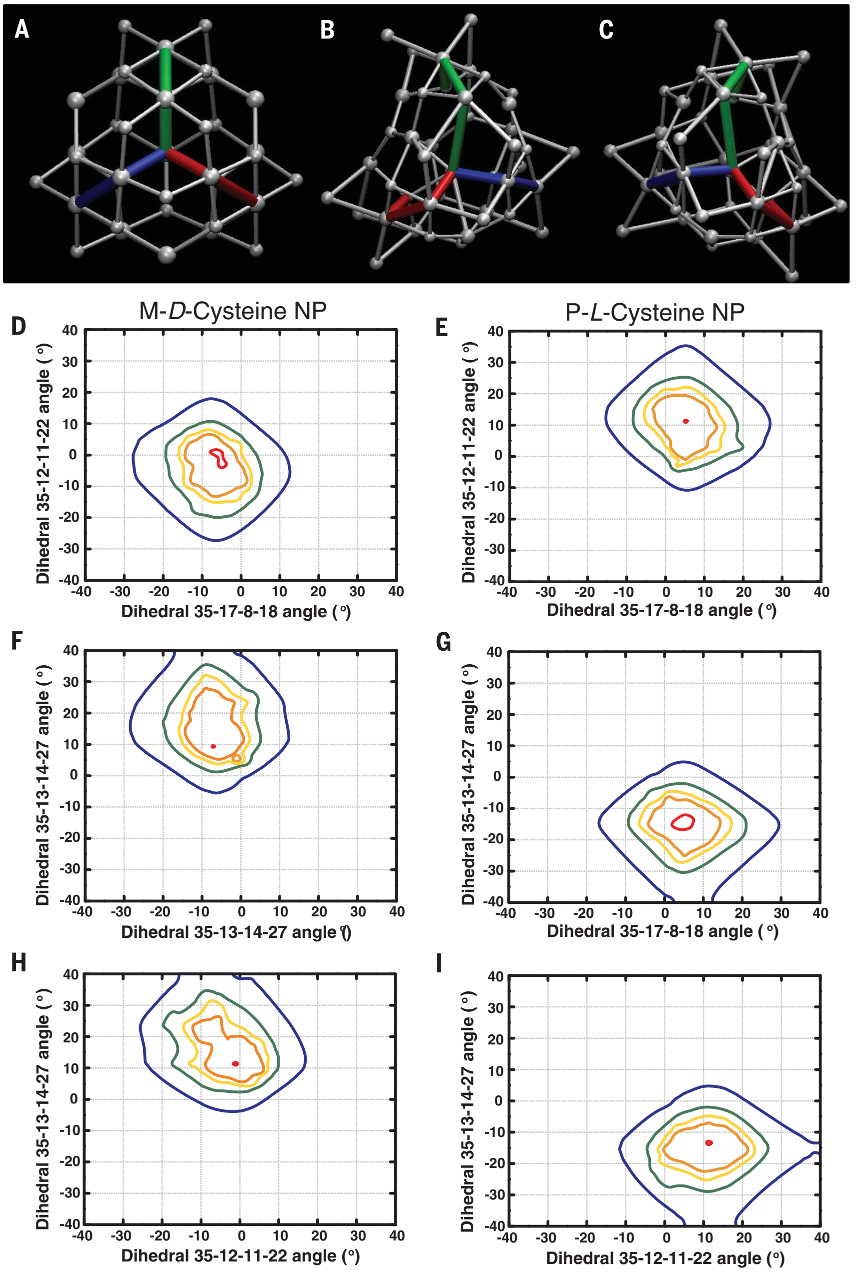

Fig. 3. Computed atomic geometry of chiral nanoparticles. (**A** to **C**) Graphical representation of the dihedral angles formed by four atoms: $\phi_{35\text{-}12\text{-}11\text{-}22}$ (red), $\phi_{35\text{-}17\text{-}8\text{-}18}$ (blue), and $\phi_{35\text{-}13\text{-}14\text{-}27}$ (green). A detailed description of the atomic types and numbering of each dihedral angle may be found in fig. S21. (A) NP with ideal crystallographic structure. (B) NP with *M*-D-Cys after 2000 fs of MD simulation. (C) NP with *P*-L-Cys after 2000 fs of MD simulation. The direction from the S atom to the carbonyl atom in the Cys molecules is taken as the basis for the geometry classification according to the Cahn-Ingold-Prelog rules. Ligands have been omitted for clarity. (**D** to **I**) Ramachadran plots for chiral NPs: two-dimensional probability maps for the relative orientation of adjoining octahedra pairs sharing the O atom number 35. Average probabilities were computed along the 2000-fs MD simulation for the NP functionalized with either *M*-D-Cys (left) or *P*-L-Cys (right). The isovalues depicted in the plots are probabilities of 0.0002 (blue), 0.0003 (green), 0.0004 (yellow), 0.0005 (orange), and 0.001 (red).

Although these experiments contain components of light-matter interactions from “natural” CD, the Faraday effect, and MCD (*29*), magneto-optical Kerr effects are unlikely to have a substantive contribution (*39*). Magnetic field–induced transparency for circularly polarized light originates in the decrease of the absorption cross section of the NPs when the magnetic field is applied in noncubic crystal lattices (*60*), and not from plasmonic effects; the latter have a different mechanism and smaller magnitude (*53*–*55*, *61*). The chiral distortions caused by the L- and D-Cys attachment to the surface of Co_3O_4 NPs make the dielectric permittivity and magnetic susceptibility tensors strongly anisotropic. The external magnetic field polarizes the paramagnetic NPs so that the spin and orbital magnetic moments become preferentially oriented in the direction of the field. The effect would be small for NPs with crystal lattices of high symmetry (e.g., cubic), and their experimental observation would require low temperatures to mitigate thermal broadening of the chiroptical peaks, because dielectric permittivity and magnetic susceptibility tensors are less anisotropic. In our observations, the transparency increase was minimal in DL-Cys NPs where chiral distortions were being partially compensated (Fig. 1A and fig. S28). The effect was also minimal for optical transitions involving surface states because the near-spherical symmetry of NPs averages the effect of external polarization on all the terms in Eq. 1. Consequently, the visible part of the CD spectra (>450 nm) of both D- and L-Cys NPs experiences little influence of the magnetic field, despite the high *g*-factor (Fig. 1B). However, the spectral region associated with Co(II)→Co(III) electronic transitions displays very strong effects because the external magnetic field forces both donor and acceptor states to become polarized simultaneously, and that is not averaged in the individual NPs or their ensembles. A simplified reason behind the reduced absorption cross section for the circularly polarized light could be the alignment of the transient magnetic moment for the Co(II)→Co(III) transition along the external magnetic field, which makes it orthogonal to the magnetic moment of incident photons, leading to a markedly reduced amplitude of the $\langle \Psi_a | \hat{\mathbf{m}} | \Psi_0 \rangle$ term.

The strong absorbance drop enables real-time optical modulation using a magnetic field, which was observed with excellent fidelity for 60 cycles (Fig. 4E); no agglomeration of NPs was observed. Cyclic switching of the gel transparency in the UV absorption band of NPs can also be converted into the modulation of photons in the visible range by using fluorescent targets (Fig. 4, D and F, and scheme S2).

Structural design of chiral NPs aimed at the maximization of the transient magnetic moment contribution to the NPs’ circular dichroism resulted in a large increase of the *g*-factor in the visible range of wavelengths and intense magnetic field–induced light modulation in the UV range. Data obtained in this study indicate that ceramic NPs with structural chirality and magnetism can be expanded to a large family of nanoscale materials with tunable chiroptical, magnetic, and other properties, enabled by the well-known tolerance of metal oxides to partial metal substitution. In addition to their technological relevance to magneto- and opto-electronic devices, the ceramic chiromagnetic NPs based on metal oxides offer a versatile experimental system for different fields of science and fundamental problems unified by chiral properties of nanoscale matter.

Corrected 29 January 2018. See full text.

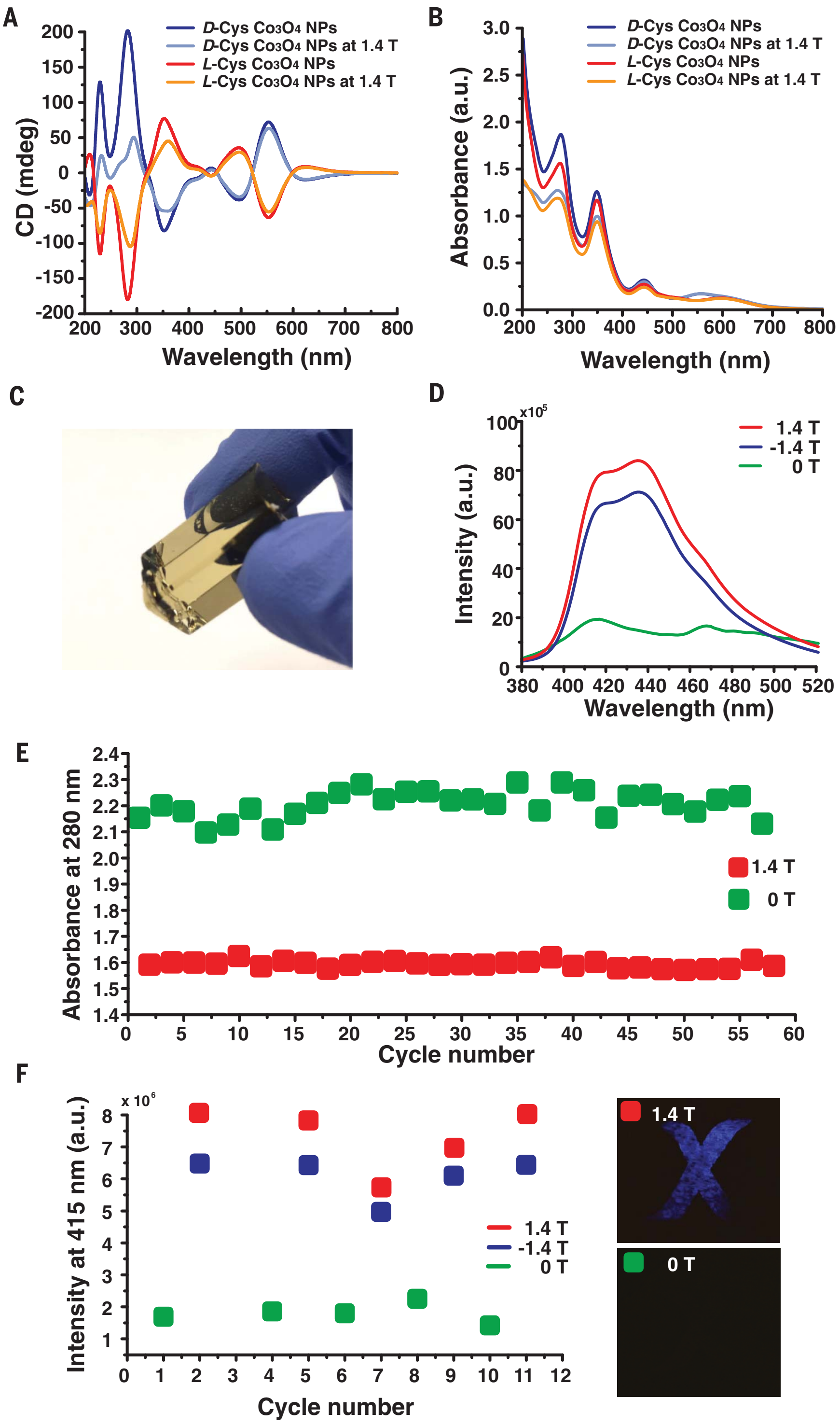

Fig. 4. Optical modulation. (**A** and **B**) CD and MCD (A) and corresponding absorbance spectra (B) of L-Cys and D-Cys Co_3O_4 NPs. (**C**) Photograph of the optically transparent gel made from L-Cys Co_3O_4 NPs. (**D**) Emission intensities of fluorescent paper plus the NP gel in front, with a magnetic field applied to the NP gel (red and blue) and without a magnetic field (green) (excitation, 280 nm). (**E**) Cycling performance of the NP gel's absorbance at 280 nm with and without magnetic fields. (**F**) Cycling profile of emission intensity at 415 nm with and without magnetic fields and corresponding photographs of blue-emitting light from the fluorescent paper.

REFERENCES AND NOTES

1. S. Bordács *et al.*, *Nat. Phys.* **8**, 734–738 (2012).
2. L. D. Barron, *Nat. Mater.* **7**, 691–692 (2008).
3. R. Naaman, D. H. Waldeck, *Annu. Rev. Phys. Chem.* **66**, 263–281 (2015).
4. C. Pfleiderer *et al.*, *J. Phys. Condens. Matter* **22**, 164207 (2010).
5. G. L. Rikken, E. Raupach, *Nature* **405**, 932–935 (2000).
6. A. O. Govorov, Z. Fan, P. Hernandez, J. M. Slocik, R. R. Naik, *Nano Lett.* **10**, 1374–1382 (2010).
7. T. Bruhn *et al.*, *Angew. Chem. Int. Ed.* **53**, 14592–14595 (2014).
8. W. Moffitt, A. Moscowitz, *J. Chem. Phys.* **30**, 648–660 (1959).
9. K. Nakanishi, R. W. W. N. Berova, *Circular Dichroism: Principles and Applications* (Wiley-VCH, 2000).
10. Y. Kitagawa, H. Segawa, K. Ishii, *Angew. Chem. Int. Ed.* **50**, 9133–9136 (2011).
11. G. L. Rikken, E. Raupach, *Nature* **390**, 493–494 (1997).
12. J. F. Hochepied, P. Sainctavit, M. P. Pileni, *J. Magn. Magn. Mater.* **231**, 315–322 (2001).
13. C. Train, M. Gruselle, M. Verdaguer, *Chem. Soc. Rev.* **40**, 3297–3312 (2011).
14. R. Sessoli *et al.*, *Nat. Phys.* **11**, 69–74 (2015).
15. C. Train *et al.*, *Nat. Mater.* **7**, 729–734 (2008).
16. M. P. Moloney, J. Govan, A. Loudon, M. Mukhina, Y. K. Gun'ko, *Nat. Protoc.* **10**, 558–573 (2015).
17. A. G. Mark, J. G. Gibbs, T.-C. Lee, P. Fischer, *Nat. Mater.* **12**, 802–807 (2013).
18. K. M. McPeak *et al.*, *Nano Lett.* **14**, 2934–2940 (2014).
19. P. K. Jain, Y. Xiao, R. Walsworth, A. E. Cohen, *Nano Lett.* **9**, 1644–1650 (2009).
20. V. Yannopapas, A. G. Vanakaras, *ACS Photonics* **2**, 1030–1038 (2015).
21. J. Crassous, *Chem. Soc. Rev.* **38**, 830–845 (2009).
22. M. V. Mukhina *et al.*, *Nano Lett.* **15**, 2844–2851 (2015).
23. C. E. Román-Velázquez, C. Noguez, I. L. Garzón, *J. Phys. Chem. B* **107**, 12035–12038 (2003).
24. S. Sun *et al.*, *J. Am. Chem. Soc.* **126**, 273–279 (2004).
25. J.-H. Lee *et al.*, *Nat. Nanotechnol.* **6**, 418–422 (2011).
26. N. Lee, T. Hyeon, *Chem. Soc. Rev.* **41**, 2575–2589 (2012).
27. J. Kumar, T. Kawai, T. Nakashima, *Chem. Commun. (Camb.)* **53**, 1269–1272 (2017).
28. T. Goto *et al.*, *Angew. Chem. Int. Ed.* **56**, 2989–2993 (2017).
29. L. D. Barron, J. Vrbancich, *Mol. Phys.* **51**, 715–730 (1984).
30. G. D. Fasman, *Circular Dichroism and the Conformational Analysis of Biomolecules* (Springer US, 1996).
31. A. Kuzyk *et al.*, *Nature* **483**, 311–314 (2012).
32. W. Chen *et al.*, *Nano Lett.* **9**, 2153–2159 (2009).
33. A. Ben-Moshe, B. M. Maoz, A. O. Govorov, G. Markovich, *Chem. Soc. Rev.* **42**, 7028–7041 (2013).
34. A. Guerrero-Martínez *et al.*, *Angew. Chem. Int. Ed.* **50**, 5499–5503 (2011).
35. J. K. Gansel *et al.*, *Science* **325**, 1513–1515 (2009).
36. A. Kuzyk *et al.*, *Nat. Mater.* **13**, 862–866 (2014).
37. Y. Kim *et al.*, *Nat. Mater.* **15**, 461–468 (2016).
38. G. Singh *et al.*, *Science* **345**, 1149–1153 (2014).
39. Supplementary materials.
40. E. L. Salabaş, A. Rumplecker, F. Kleitz, F. Radu, F. Schüth, *Nano Lett.* **6**, 2977–2981 (2006).
41. S. Haffer, T. Walther, R. Köferstein, S. G. Ebbinghaus, M. Tiemann, *J. Phys. Chem. C* **117**, 24471–24478 (2013).
42. A. B. Buda, K. Mislow, *J. Am. Chem. Soc.* **114**, 6006–6012 (1992).
43. T. Risthaus, A. Hansen, S. Grimme, *Phys. Chem. Chem. Phys.* **16**, 14408–14419 (2014).
44. N. Nishida, H. Yao, T. Ueda, A. Sasaki, K. Kimura, *Chem. Mater.* **19**, 2831–2841 (2007).
45. Y. Zhou *et al.*, *Angew. Chem. Int. Ed.* **50**, 11456–11459 (2011).
46. T. Nakashima, Y. Kobayashi, T. Kawai, *J. Am. Chem. Soc.* **131**, 10342–10343 (2009).
47. G. Wang *et al.*, *J. Phys. Chem. C* **113**, 4357–4361 (2009).
48. L. A. Nafie, *Chem. Phys.* **205**, 309–322 (1996).
49. Y. Fujioka, J. Frantti, A. Puretzky, G. King, *Inorg. Chem.* **55**, 9436–9444 (2016).
50. B. L. A. Harman, I. Sóvágó, *Inorg. Chim. Acta* **80**, 75–83 (1983).
51. Y. Ikedo *et al.*, *Phys. Rev. B* **75**, 054424 (2007).
52. J. L. Alonso-Gómez, P. Rivera-Fuentes, N. Harada, N. Berova, F. Diederich, *Angew. Chem. Int. Ed.* **48**, 5545–5548 (2009).

53. B. Han *et al.*, *Nano Lett.* **17**, 6083–6089 (2017).
54. H. Yao, Y. Ishikawa, *J. Phys. Chem. C* **119**, 13224–13230 (2015).
55. H. Yao, T. Shiratsu, *Nanoscale* **8**, 11264–11274 (2016).
56. F. Pineider *et al.*, *Nano Lett.* **13**, 4785–4789 (2013).
57. D. A. Kuzmin, I. V. Bychkov, V. G. Shavrov, V. V. Temnov, *Nano Lett.* **16**, 4391–4395 (2016).
58. J. H. Yu *et al.*, *Nat. Mater.* **9**, 47–53 (2010).
59. N. Norberg, D. Gamelin, *J. Appl. Phys.* **99**, 08M104 (2006).
60. J. Li *et al.*, *Opt. Mater. Express* **2**, 1760 (2012).
61. I. Zubritskaya *et al.*, *Nano Lett.* 10.1021/acs.nanolett.7b04139 (2017).

ACKNOWLEDGMENTS

All data are reported in the main text and supplementary materials. The central part of this work was supported by the NSF Ceramics program through the project "Ceramics quasicrystals" (grant no. 1411014). Partial support of this work was also provided by the NSF-funded project "Energy- and cost-efficient manufacturing employing nano-particles" (grant no. 1463474) and the Air Force Office of Scientific Research–funded project "Nanocomposite ion conductors from branched aramid nanofibers" (grant no. FA9550-16-1-0265). We also thank the Brazilian funding agencies Coordenação de Aperfeiçoamento de Pessoal de Nível Superior (CAPES), Conselho Nacional de Desenvolvimento Científico e Tecnológico (CNPq), and Fundação de Amparo à Pesquisa do Estado de São Paulo (FAPESP; grants 2012/15147-4 and 2013/07296-2) for financial support. The authors acknowledge the National Laboratory for Scientific Computing (LNCC/MCTI, Brazil) for providing the high-performance computing resources of the SDumont supercomputer (http://sdumont.lncc.br), which have contributed to the results reported in this paper. A.F.d.M. thanks Ministério da Educação/Programa de Educação Tutorial for a fellowship. U.S.S. thanks CNPq for a scholarship. M.Che. acknowledges the support of the Swiss National Science Foundation Early Postdoc Mobility Fellowship (grant no. P2GEP2-165061).

SUPPLEMENTARY MATERIALS

www.sciencemag.org/content/359/6373/309/suppl/DC1
Materials and Methods
Figs. S1 to S33
Tables S1 to S15
Schemes S1 to S3
References (*62*–*94*)
Movies S1 to S5

8 September 2017; accepted 4 December 2017
10.1126/science.aao7172

Science

Chiromagnetic nanoparticles and gels

Jihyeon Yeom, Uallisson S. Santos, Mahshid Chekini, Minjeong Cha, André F. de Moura and Nicholas A. Kotov

Science **359** (6373), 309-314.
DOI: 10.1126/science.aao7172

Boosting chiral nanoparticle responses

Optical nanomaterials that combine chirality and magnetism are useful for magneto-optics and as chiral catalysts. Although chiral inorganic nanostructures can exhibit high circular dichroism, modulating this optical activity has usually required irreversible chemical changes. Yeom *et al.* synthesized paramagnetic cobalt oxide (Co_3O_4) nanoparticles with l- and d-cysteine surface ligands. These ligands created chiral distortions of the crystal lattices, and this anisotropy led to much stronger chiroptical activity. The circular dichroism in the ultraviolet of nanoparticle gels could be modulated with magnetic fields of ~1.5 tesla.

Science, this issue p. 309

Science (print ISSN 0036-8075; online ISSN 1095-9203) is published by the American Association for the Advancement of Science, 1200 New York Avenue NW, Washington, DC 20005.